Supporting Information

Modulating The Relaxation Dynamics Via Structural Transition From Dinuclear Dysprosium Cluster To Nonanuclear Cluster

Peng Hu, [a,b] Ling-hui Cao,[b] Ao-gang Liu,[b] Yi-quan Zhang,*[c] Tian-le Zhang,*[b] Bao Li,*[b]

[a]Hubei Key Laboratory of Radiation Chemistry and Functional Materials, Non-power Nuclear Technology Collaborative Innovation Center, Hubei University of Science and Technology, Xianning, 437100, People's Republic of China.

[b]Key laboratory of Material Chemistry for Energy Conversion and Storage, School of Chemistry and Chemical Engineering, Huazhong University of Science and Technology, Wuhan, 430074，People's Republic of China. Email: libao@hust.edu.cn; tlzhang@hust.edu.cn.

[c]Jiangsu Key Laboratory for NSLSCS, School of Physical Science and Technology, Nanjing Normal University, Nanjing, 210023, People's Republic of China. E-mail: zhangyiquan@njnu.edu.cn

Table S1 Crystal data and structure refinements for complexes **1** and **2**.

	1	2
Chemical formula	$C_{20}H_{28}Dy_2N_6O_{20}$	$C_{36}H_{68}Dy_9N_8O_{58}$
Formula Mass	997.48	3003.48
Crystal system	Triclinic	Orthorhombic
a/ Å	9.0925(2)	15.328(3)
b/ Å	9.5016(2)	17.913(4)
c/ Å	11.1478(2)	18.551(4)
α/°	68.381(2)	90
β/°	82.643(2)	90
γ/°	67.042(2)	90
Unit cell volume/Å^3	824.29(3)	5093.3(18)
Temperature/K	294.5(3)	293(2)
Space group	$P\text{-}1$	$I222$
Z	1	2
No. of reflections measured	3195	4494
No. of independent reflections	3195	4494
R_{int}	0.0211	0.0965
Final R_1 values ($I > 2\sigma(I)$)	0.0189	0.0612
Final $wR(F^2)$ values ($I > 2\sigma(I)$)	0.0516	0.1661
Final R_1 values (all data)	0.0200	0.0614
Final $wR(F^2)$ values (all data)	0.0521	0.1666
CCDC	1577365	2085775

$^a R_1 = \sum ||F_o| - |F_c||/ \sum |F_o|$. $^b wR_2 = [\sum w(F_o^2 - F_c^2)^2/\sum w(F_o^2)^2]^{1/2}$.

**Table S2** Selected bond lengths (Å) and bond angles (°) for **1**.

1 / Å			
Dy1-O1 2.5082(19)	Dy1-O1W 2.3711(19)	Dy1-O2 2.2583(17)	Dy1-O2 2.2837(16)
Dy1-O3 2.4945(19)	Dy1-O4 2.450(2)	Dy1-O6 2.420(2)	Dy1-O7 2.512(2)
Dy1-O9 2.444(2)	Dy1-Dy1 3.8056(3)		
1 / °			
O2-Dy1-O1 131.84(6)	O2-Dy1-O1 65.88(6)	O2-Dy1-O1W 140.01(7)	O2-Dy1-O1W 145.97(8)
O2-Dy1-O2 66.17(7)	O2-Dy1-O3 130.66(6)	O2-Dy1-O3 66.51(6)	O2-Dy1-O4 78.01(7)
O2-Dy1-O4 78.79(7)	O2-Dy1-O6 124.69(7)	O2-Dy1-O6 117.16(7)	O2-Dy1-O7 105.75(7)
O2-Dy1-O7 76.87(7)	O2-Dy1-O9 75.61(7)	O2-Dy1-O9 101.12(7)	O2-Dy1-O9 101.12(7)
O4-Dy1-O1 87.39(8)	O4-Dy1-O3 80.03(8)	O4-Dy1-O7 151.05(8)	O6-Dy1-O1 75.34(8)
O6-Dy1-O3 80.11(8)	O9-Dy1-O1 70.93(7)	O7-Dy1-Dy1#1 91.61(5)	O9-Dy1-Dy1#1 88.01(5)

**Table S3** Selected bond lengths (Å) and bond angles (°) for **2**.

2 / Å			
Dy1-O10 2.384(13)	Dy1-O11 2.403(13)	Dy1-O10#1 2.384(13)	Dy1-O11#1 2.403(13)
Dy2-O1 2.603(14)	Dy2-O2 2.273(14)	Dy2-O4 2.307(16)	Dy2-O6 2.533(2)
Dy2-O10 2.338(12)	Dy2-O11 2.328(13)	Dy2-O12 2.527(16)	Dy2-O14 2.499(17)
Dy2-O15 2.428(18)	Dy3-O2 2.290(13)	Dy3-O3 2.675(15)	Dy3-O4 2.276(15)
Dy3-O5 2.371(15)	Dy3-O6 2.546(2)	Dy3-O7 2.562(14)	Dy3-O8 2.481(17)
Dy3-O10 2.331(13)	Dy3-O11 2.320(11)	Dy1-Dy2 3.7645(9)	Dy2-Dy3 3.5208(13)
2 / °			
O10-Dy1-O11 72.7(4)	O10-Dy1-O11#1 80.8(4)	O10-Dy1-O11#2 71.9(4)	O10-Dy1-O11#3 140.1(4)
O10-Dy1-O10#1 78.9(6)	O10-Dy1-O10#2 111.8(6)	O10-Dy1-O10#3 145.2(6)	O2-Dy2-O12 121.6(5)
O2-Dy2-O14 83.3(6)	O2-Dy2-O15 145.4(5)	O10-Dy2-O14 88.5(5)	O11-Dy2-Dy3 95.6(3)
O11-Dy2-O1 151.8(5)	O12-Dy2-O1 116.5(5)	O12-Dy2-O6 131.8(5)	O15-Dy2-O1 82.6(6)
O2-Dy3-O5 138.4(5)	O2-Dy3-O6 67.6(4).	O4-Dy3-O6 67.6(5)	O4-Dy3-O7 132.3(7)
O5-Dy3-O3 76.2(6) -	O5-Dy3-O6 139.3(4)	O8-Dy3-O6 139.2(4)	O8-Dy3-O7 51.8(5)
O10-Dy3-O5 141.2(5)	O10-Dy3-O6 66.0(4)	O11-Dy3-O3 154.7(5)	O11-Dy3-O5 89.3(5)
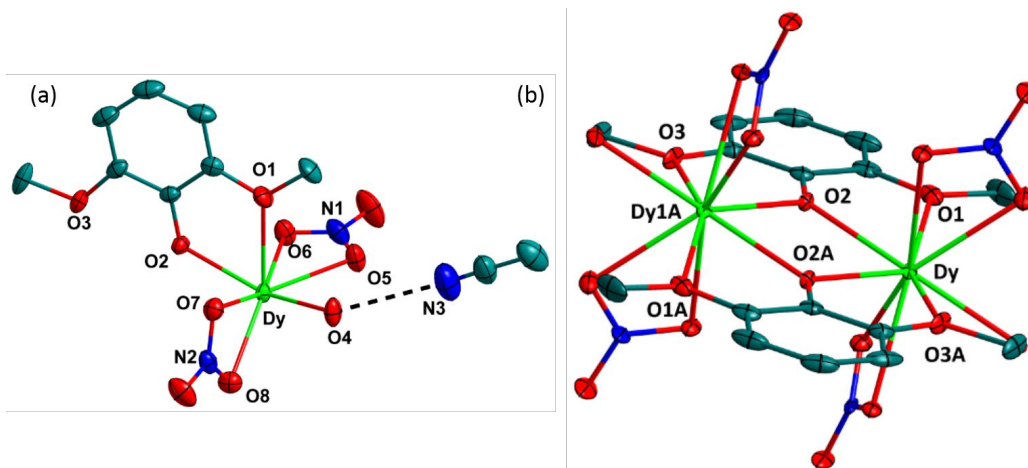
Figure S1. (a) Perspective view of the asymmetric unit of compound **1** with acetonitrile molecules; (b) ORTEP representation of **1** with the thermal ellipsoids at 30% probability. Hydrogen atoms are omitted for clarity. Color code: Dy, bright green; O, red; N, blue; C, teal.
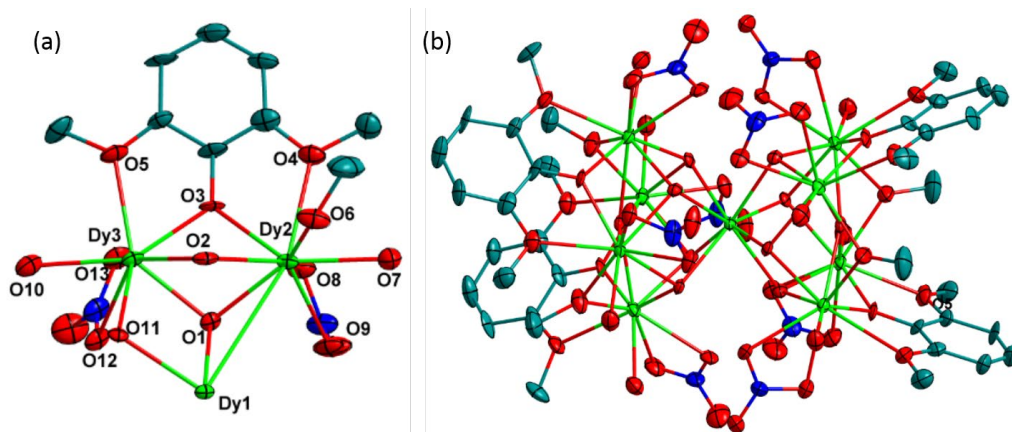
Figure S2. (a) Perspective view of the asymmetric unit of compound **2** with methanol molecules; (b) ORTEP representation of **2** with the thermal ellipsoids at 30% probability. Hydrogen atoms are omitted for clarity. Color code: Dy, bright green; O, red; N, blue; C, teal.
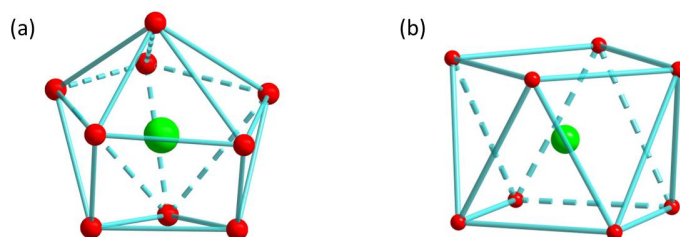
Figure S3. (a) The coordination geometry of Dy^{III} ion in compound **1**; (b) The coordination geometry of Dy^{III}(1) ion in compound **2**. Color code: Dy, bright green; O, red.

Table S4 The evaluated local coordination geometry analysis for Dy^{III} ion in compound **1** by

SHAPE software.

Label	Shape	Symmetry	Distortion(°)
EP-9	D_{9h}	Enneagon	34.475
OPY-9	C_{8v}	Octagonal pyramid	23.361
HBPY-9	D_{7h}	Heptagonal bipyramid	17.623
JTC-9	C_{3v}	Johnson triangular cupola J3	15.068
JCCU-9	C_{4v}	Capped cube J8	9.473
CCU-9	C_{4v}	Spherical-relaxed capped cube	9.110
JCSAPR-9	C_{4v}	Capped square antiprism J10	1.833
CSAPR-9	C_{4v}	**Spherical capped square antiprism**	**1.281**
JTCTPR-9	D_{3h}	Tricapped trigonal prism J51	2.457
TCTPR-9	D_{3h}	Spherical tricapped trigonal prism	2.424
JTDIC-9	C_{3v}	Tridiminished icosahedron J63	11.348
HH-9	C_{2v}	Hula-hoop	11.384
MFF-9	C_s	Muffin	1.714

Table S5 The evaluated local coordination geometry analysis for $Dy^{III}(1)$ ion in compound **2** by

SHAPE software.

Label	Shape	Symmetry	Distortion(°)
OP-8	D_{8h}	Octagon	30.509
HPY-8	C_{7v}	Heptagonal pyramid	23.602
HBPY-8	D_{6h}	Hexagonal bipyramid	16.148
CU-8	O_h	Cube	8.836
SAPR-8	D_{4d}	**Square antiprism**	**0.304**
TDD-8	D_{2d}	Triangular dodecahedron	2.341
JGBF-8	D_{2d}	Johnson gyrobifastigium J26	16.498
JETBPY-8	D_{3h}	Johnson elongated triangular bipyramid J14	29.363

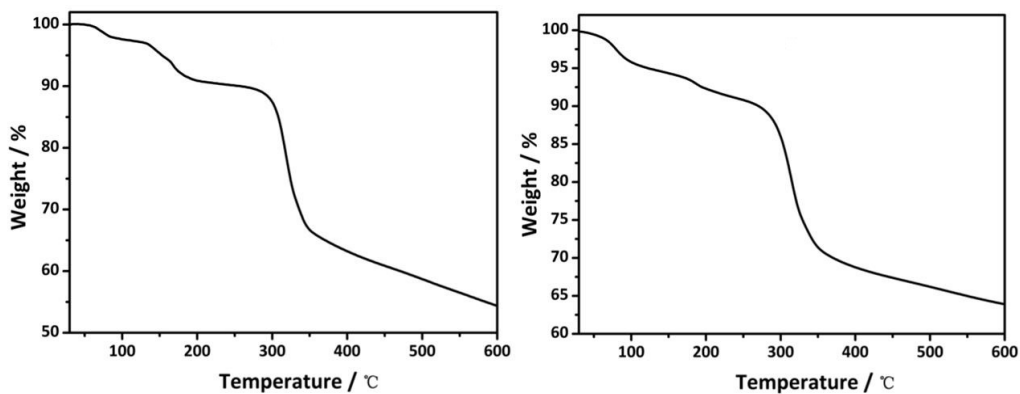| JBTPR-8 | C_{2v} | Biaugmented trigonal prism J50 | 2.903 |
BTPR-8	C_{2v}	Biaugmented trigonal prism	2.366
JSD-8	D_{2d}	Snub diphenoid J84	5.294
TT-8	T_d	Triakis tetrahedron	9.705
ETBPY-8	D_{3h}	Elongated trigonal bipyramid	24.997
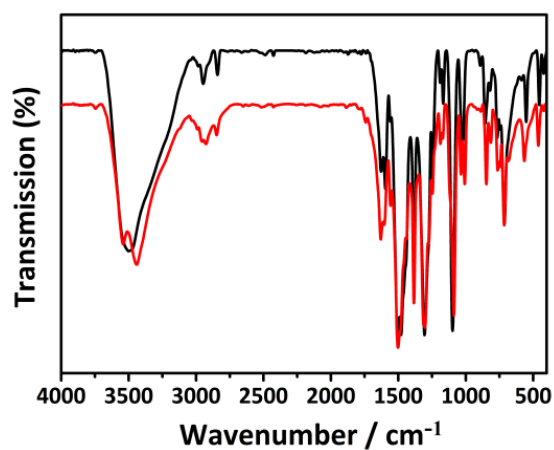
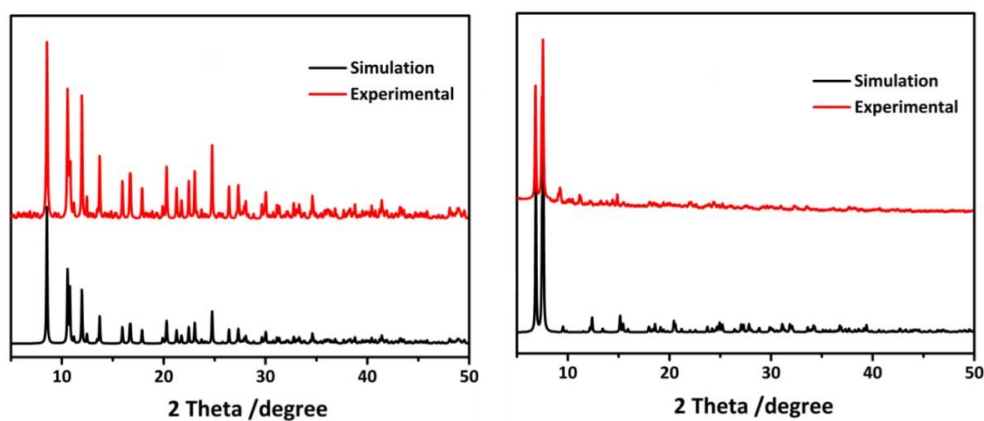**Figure S4.** FT-IR spectra of compounds **1** (black) and **2** (red).

**Figure S5.** TG curves of compounds **1** (left) and **2** (right).

Figure S6. The simulated X-ray powder diffraction patterns (black) and the experimental ones (red) of compounds **1** (left) and **2** (right). The experimental PXRD patterns are primarily consistent with the the corresponding simulated ones, highlighting the phase purity of the four complexes. Minor inconsistencies in the intensity and shape of the peaks were observed between the experimental and simulation data due to the different orientations of the crystal samples.
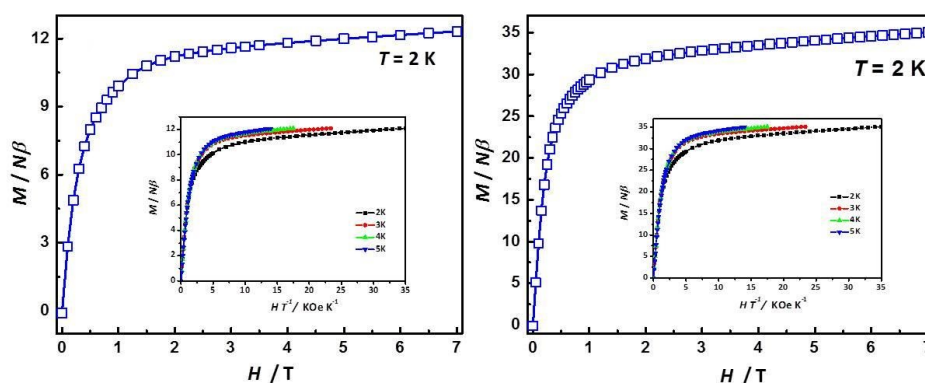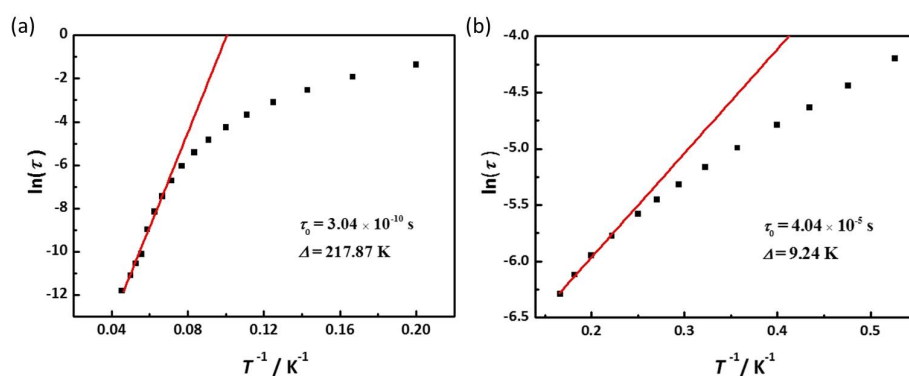

Figure S7. Magnetization curve for compounds **1** (left) and **2** (right) at 2 K. Inset: *M vs. H/T* plots at different temperatures (2 K, 3 K, 4 K and 5 K).
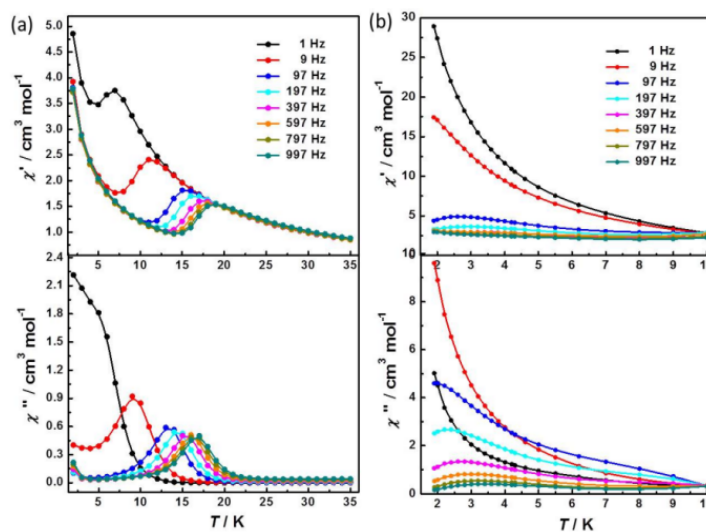
Figure S8. Temperature dependence of the in-phase (χ') and out-of-phase (χ'') ac susceptibilities of **1** (a) and **2** (b) under zero dc field.
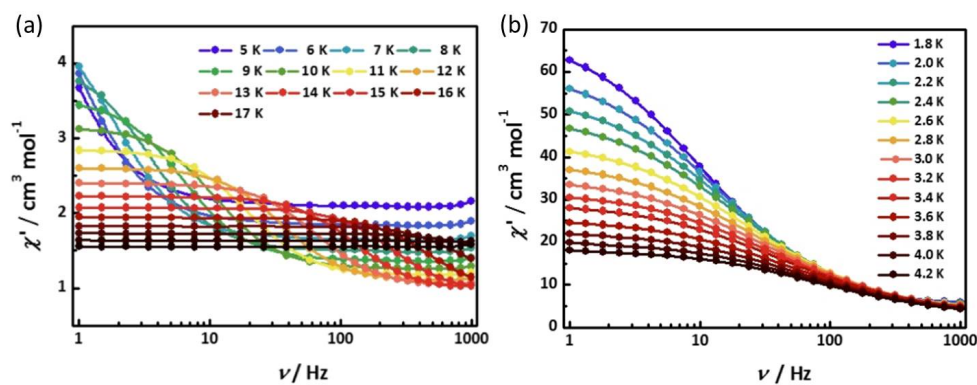
Figure S9. Frequency dependence of the in-phase (χ') ac susceptibilities of **1** (a) and **2** (b) under zero dc field.

Figure S10. Arrhenius plots of relaxation time data for **1** (a) and **2** (b). Solid red lines correspond to the best fits in the high-temperature regime.

Table S6. The parameters obtained by fitting Cole-Cole plot under zero dc field for **1**.

T (K)	χ_S	χ_T	τ	α
5	2.10	6.92	0.26	0.10
6	1.84	5.56	0.15	0.077
7	1.65	4.63	0.080	0.053
8	1.37	4.00	0.045	0.042
9	1.26	3.52	0.025	0.035
10	1.17	3.15	0.014	0.031
11	1.09	2.86	0.80E-02	0.033
12	1.02	2.61	0.44E-02	0.032
13	0.95	2.41	0.24E-02	0.034

14	0.88	2.23	0.12E-02	0.036
15	0.81	2.08	0.59E-03	0.038
16	0.65	1.95	0.29E-03	0.039
17	0.027	1.83	0.13E-03	0.047
18	0.087	1.73	0.40E-04	0.062
19	0.12E-12	1.64	0.27E-04	0.79E-15
20	0.17E-12	1.56	0.15E-04	0.21E-14

Table S7. The parameters obtained by fitting Cole-Cole plot under zero dc field for **2**.

T (K)	χ_S	χ_T	τ	α
1.8	3.97	70.0	0.015	0.32
2.0	3.60	61.8	0.012	0.33
2.2	3.33	55.6	0.0097	0.34
2.4	3.14	50.8	0.0083	0.35
2.6	2.90	44.6	0.0068	0.36
2.8	2.75	39.8	0.0057	0.37
3.0	2.62	35.8	0.0049	0.38
3.3	2.53	32.6	0.0043	0.38
3.6	2.45	29.8	0.0038	0.39
4.0	2.33	26.0	0.0031	0.39
4.5	2.24	23.0	0.0026	0.39
5.0	2.16	20.6	0.0022	0.38

Computational details

Complex **1** has one type of Dy^{III}, and **2** has two types of Dy^{III}, thus one and two Dy^{III} fragments for **1** and **2** were calculated, respectively. Complete-active-space self-consistent field (CASSCF) calculations on individual lanthanide Dy^{III} fragments of model structures (see Figure S11 for the calculated model structures of **1**, **2**_*a*, **2**_*b*).

The complete structures of the two complexes extracted from the compounds on the basis of single-crystal X-ray determined geometries have been carried out with MOLCAS 8.2 program package.[S1] Central Dy^{III} fragment was calculated keeping the experimentally determined structure of the corresponding compound while replacing the other Dy^{III} ions by diamagnetic Lu^{III}. In the calculation of the other type of Dy^{III} fragment, the influence of the central Dy^{III} ion was taken into account by the closed-shell Lu^{III} *ab initio* embedding model potentials (AIMP; La.ECP.deGraaf.0s.0s.0e-La-(LaMnO3.).[S2]

The basis sets for all atoms are atomic natural orbitals from the MOLCAS ANO-RCC library: ANO-RCC-VTZP for Dy^{III} ion; VTZ for close O; VDZ for distant atoms. The calculations employed the second order Douglas-Kroll-Hess Hamiltonian, where scalar relativistic contractions were taken into account in the basis set and the spin-orbit couplings were handled separately in the restricted active space state interaction (RASSI-SO) procedure. For the fragment of individual Dy^{III} ion, active electrons in 7 active orbitals include all f electrons (CAS (9 in 7)) in the CASSCF calculation. To exclude all the doubts, we calculated all the roots in the active space. We have mixed the maximum number of spin-free state which was possible with our hardware (all from 21 sextets, 128 from 224 quadruplets, 130 from 490 doublets). And then, Single_Aniso[S3] program was used to obtain the g tensors, energy levels, magnetic axes, *et al.,* based on the above CASSCF/RASSI calculations.

1
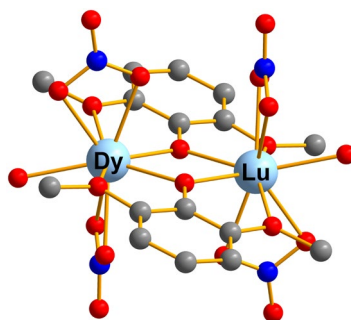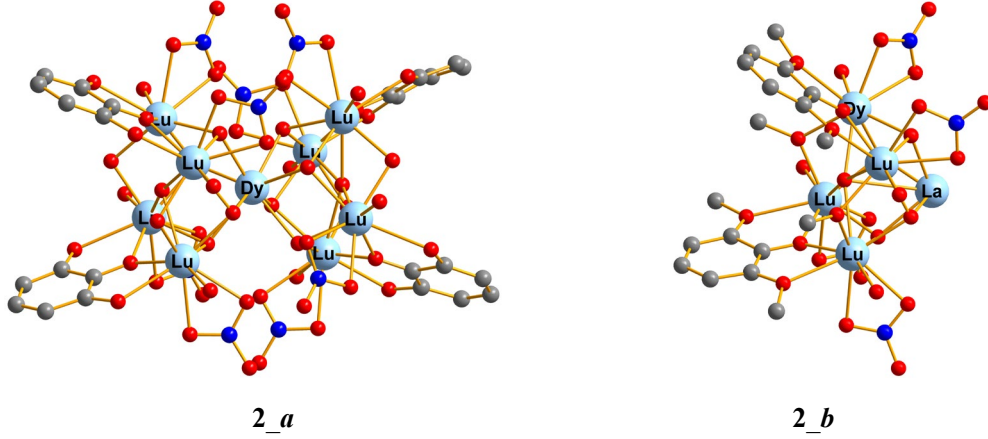
Figure S11. Calculated model structures of **1**, **2_a**, **2_b**; H atoms are omitted.

To fit the exchange interaction in complexes **1** and **2**, we took two steps to obtain them. Firstly, we calculated individual Dy^{III} fragments using CASSCF to obtain the corresponding magnetic properties. Then, the exchange interaction between the magnetic centers is considered within the Lines model,[S4] while the account of the dipole-dipole magnetic coupling is treated exactly. The Lines model is effective and has been successfully used widely in the research field of f-element single-molecule magnets.[S5]

For complex **1**, there is only one type of J.

The exchange Hamiltonian is:

$$\hat{H}_{exch} = -J\,\tilde{\hat{S}}_{Dy1}\,\tilde{\hat{S}}_{Dy1'} \tag{S1}$$

For complex **2**, there are twenty types of J.

The exchange Hamiltonian is:

$$
\begin{aligned}
\hat{H}_{exch} = &-J_1\,\tilde{\hat{S}}_{Dy1}\,\tilde{\hat{S}}_{Dy2} - J_2\,\tilde{\hat{S}}_{Dy1}\,\tilde{\hat{S}}_{Dy3} - J_3\,\tilde{\hat{S}}_{Dy1}\,\tilde{\hat{S}}_{Dy4} \\
&-J_4\,\tilde{\hat{S}}_{Dy1}\,\tilde{\hat{S}}_{Dy5} - J_5\,\tilde{\hat{S}}_{Dy1}\,\tilde{\hat{S}}_{Dy6} - J_6\,\tilde{\hat{S}}_{Dy1}\,\tilde{\hat{S}}_{Dy7} - J_7\,\tilde{\hat{S}}_{Dy1}\,\tilde{\hat{S}}_{Dy8} \\
&-J_8\,\tilde{\hat{S}}_{Dy1}\,\tilde{\hat{S}}_{Dy9} - J_9\,\tilde{\hat{S}}_{Dy2}\,\tilde{\hat{S}}_{Dy3} - J_{10}\,\tilde{\hat{S}}_{Dy3}\,\tilde{\hat{S}}_{Dy4} - J_{11}\,\tilde{\hat{S}}_{Dy4}\,\tilde{\hat{S}}_{Dy5} \\
&-J_{12}\,\tilde{\hat{S}}_{Dy2}\,\tilde{\hat{S}}_{Dy5} - J_{13}\,\tilde{\hat{S}}_{Dy2}\,\tilde{\hat{S}}_{Dy4} - J_{14}\,\tilde{\hat{S}}_{Dy3}\,\tilde{\hat{S}}_{Dy5} - J_{15}\,\tilde{\hat{S}}_{Dy6}\,\tilde{\hat{S}}_{Dy7} \\
&-J_{16}\,\tilde{\hat{S}}_{Dy7}\,\tilde{\hat{S}}_{Dy8} - J_{17}\,\tilde{\hat{S}}_{Dy8}\,\tilde{\hat{S}}_{Dy9} - J_{18}\,\tilde{\hat{S}}_{Dy6}\,\tilde{\hat{S}}_{Dy9} - J_{19}\,\tilde{\hat{S}}_{Dy6}\,\tilde{\hat{S}}_{Dy8} \\
&-J_{20}\,\tilde{\hat{S}}_{Dy7}\,\tilde{\hat{S}}_{Dy9}
\end{aligned} \tag{S2}
$$
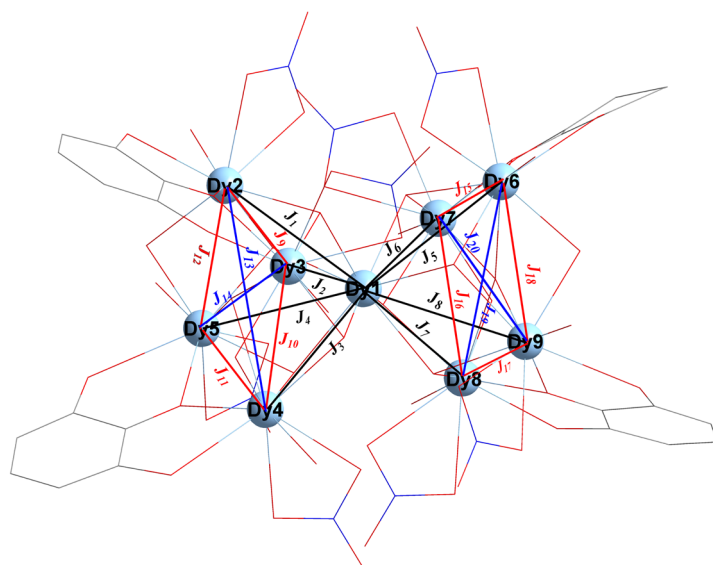
Figure S12. Labeled Dy-Dy interactions in complex **2**.

$\tilde{J} = 25\cos\varphi J$, where φ is the angle between the anisotropy axes on two Dy^{III} sites, and J is the Lines exchange coupling parameter. The $\tilde{J}_{total}$ is the parameter of the total magnetic interaction ($\tilde{J}_{total} = \tilde{J}_{dip} + \tilde{J}_{exch}$) between magnetic center ions. $\hat{\tilde{S}}_{Dy} = \pm 1/2$ is the ground pseudospin on the Dy^{III} site. The dipolar magnetic coupling can be calculated exactly, while the exchange coupling constants were fitted through comparison of the computed and measured magnetic susceptibilities.

Table S8. Calculated energy levels (cm^{-1}), **g** (g_x, g_y, g_z) tensors and m_J values of the lowest Kramers doublets (KDs) of individual Dy^{III} fragments of **1**, **2**_a and **2**_b.

	1				**2_a**				**2_b**			
KDs	E/cm^{-1}		**g**	m_J	E/cm^{-1}		**g**	m_J	E/cm^{-1}		**g**	m_J
1	0.0	g_x	0.172	±15/2	0.0	g_x	0.154	±15/2	0.0	g_x	0.183	±15/2
		g_y	0.517			g_y	0.344			g_y	0.589	
		g_z	19.061			g_z	19.574			g_z	18.818	
2	42.6	g_x	0.127	±5/2	72.0	g_x	10.715	±13/2	40.0	g_x	0.974	±13/2
		g_y	0.403			g_y	8.167			g_y	1.339	
		g_z	18.234			g_z	2.677			g_z	17.843	
3	126.5	g_x	0.399	±9/2	90.7	g_x	7.108	±7/2	85.5	g_x	2.051	±9/2
		g_y	0.820			g_y	5.828			g_y	4.197	
		g_z	16.669			g_z	3.426			g_z	13.332	
4	159.5	g_x	1.639	±13/2	107.7	g_x	9.227	±11/2	150.2	g_x	8.131	±7/2
		g_y	3.479			g_y	7.315			g_y	7.562	
		g_z	15.213			g_z	2.747			g_z	2.112	

5	179.7	g_x	0.026	±7/2	137.8	g_x	1.716	±9/2	246.0	g_x	0.408	±3/2
		g_y	5.041			g_y	3.859			g_y	4.389	
		g_z	11.201			g_z	9.191			g_z	10.011	
6	217.3	g_x	2.135	±11/2	156.8	g_x	1.760	±5/2	322.0	g_x	1.610	±11/2
		g_y	4.462			g_y	3.931			g_y	2.092	
		g_z	13.109			g_z	10.887			g_z	13.858	
7	268.3	g_x	1.147	±3/2	230.8	g_x	0.028	±3/2	421.5	g_x	0.571	±1/2
		g_y	1.630			g_y	0.039			g_y	0.651	
		g_z	14.361			g_z	16.980			g_z	16.548	
8	355.9	g_x	0.199	±1/2	674.1	g_x	0.000	±1/2	492.4	g_x	0.129	±5/2
		g_y	0.565			g_y	0.000			g_y	0.291	
		g_z	18.564			g_z	19.856			g_z	19.355	

Table S9. Fitted exchange coupling constant J_{exch}, the calculated dipole-dipole interaction J_{dip} and the total J between Dy^{III} ions in **1−2**. The intermolecular interactions zJ' of **1−2** were both fit to 0.00 cm^{-1}.

	1			2		
	J_{dip}	J_{exch}	J_{total}	J_{dip}	J_{exch}	J_{total}
J_1	1.95	3.50	5.45	−0.49	1.50	1.01
J_2				0.01	1.50	1.51
J_3				−0.72	1.50	0.78
J_4				−0.66	1.50	0.84
J_5				−0.95	1.50	0.55
J_6				−1.35	1.50	0.15
J_7				−0.34	1.50	0.16
J_8				−1.38	1.50	0.12
J_9				−4.44	0.75	−3.69
J_{10}				5.23	0.75	5.98
J_{11}				−4.25	0.75	−3.50
J_{12}				5.68	0.75	6.43
J_{13}				2.18	0.75	2.93
J_{14}				2.25	0.75	3.00
J_{15}				−3.73	0.75	−2.98
J_{16}				5.27	0.75	6.02
J_{17}				−3.82	0.75	−3.07
J_{18}				5.59	0.75	6.34
J_{19}				2.23	0.75	2.98
J_{20}				1.68	0.75	2.43

Table S10. Exchange energies (cm^{-1}) and main values of the g_z for the lowest two exchange doublets of complex **1** and the lowest eight exchange doublets of complex **2**.

	1		**2**	
	E/cm^{-1}	g_z	E/cm^{-1}	g_z
1	0.000 0.001	38.120	0.0	159.721
2	3.030 3.031	0.000	0.7	20.531
3			1.0	56.490
4			1.2	93.812
5			1.3	56.368
6			1.5	93.721
7			1.7	110.221
8			1.9	63.118

1   **2**
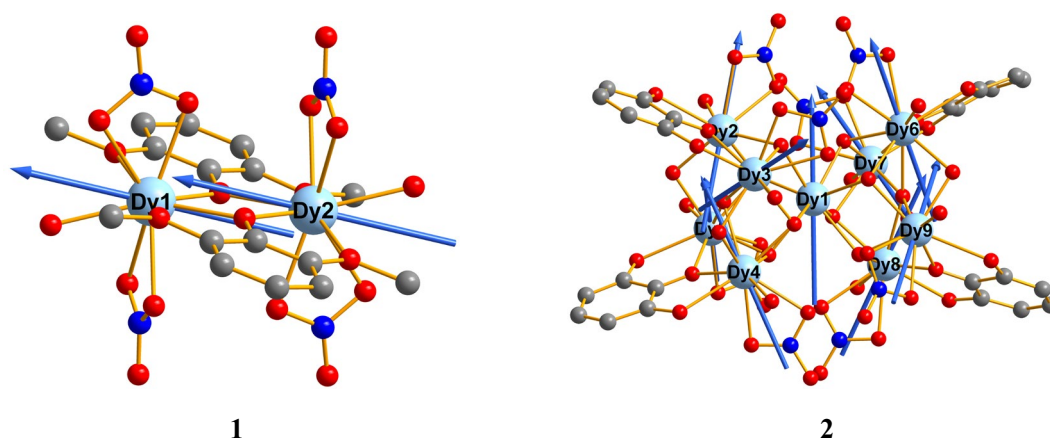
Figure S13. Calculated orientations of the local main magnetic axes of the ground Kramers (light blue) doublet on Dy^{III} ions of complexes **1** and **2**.
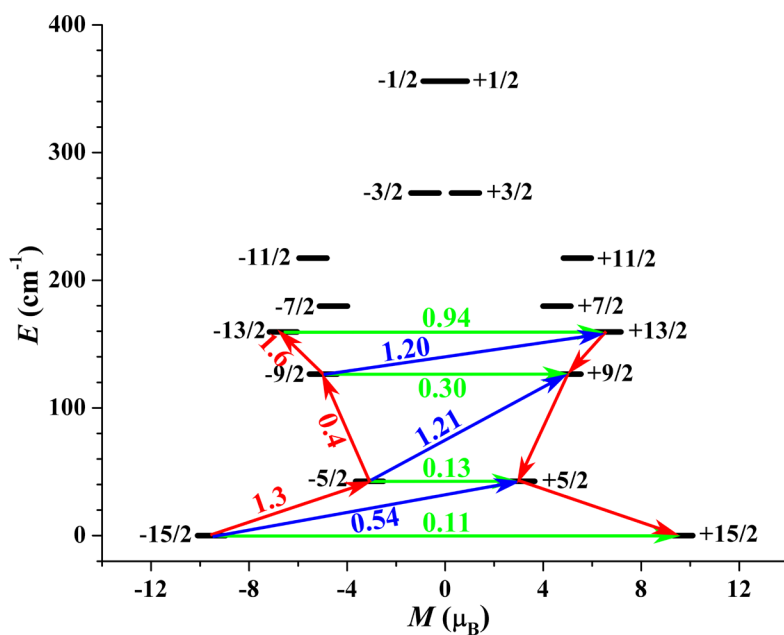
Figure S14. The magnetization blocking barriers for individual Dy^{III} fragments of **1**. The thick black lines represent the Kramers doublets as a function of their magnetic moment along the magnetic axis. The green lines correspond to diagonal quantum tunneling of magnetization (QTM); the blue line represent off-diagonal relaxation process. The numbers at each arrow stand for the mean absolute value of the corresponding matrix element of transition magnetic moment.
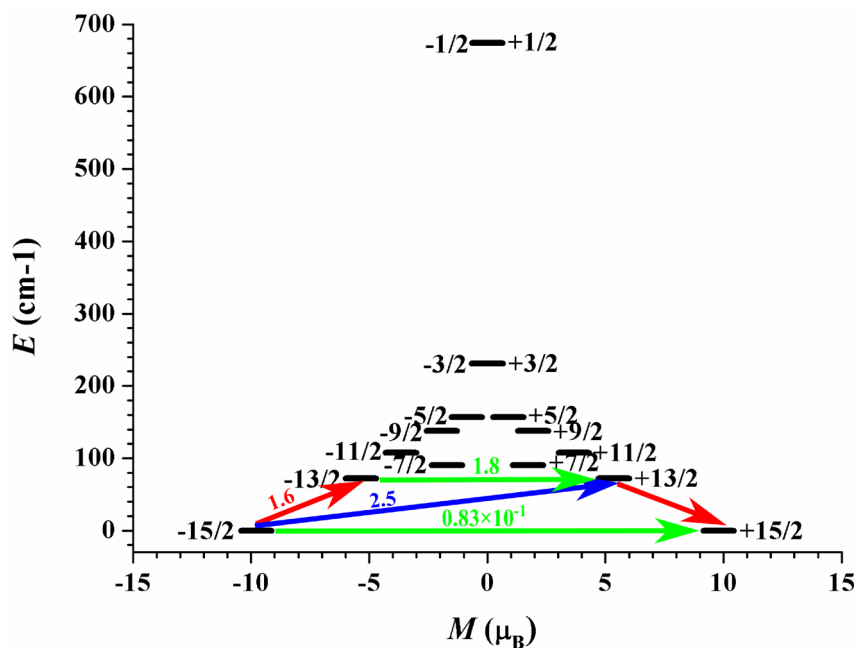
Figure S15. The magnetization blocking barriers for individual Dy^{III} fragments of **2**_a. The thick black lines represent the Kramers doublets as a function of their magnetic moment along the magnetic axis. The green lines correspond to diagonal quantum tunneling of magnetization (QTM); the blue line represent off-diagonal relaxation process. The numbers at each arrow stand for the mean absolute value of the corresponding matrix element of transition magnetic moment.
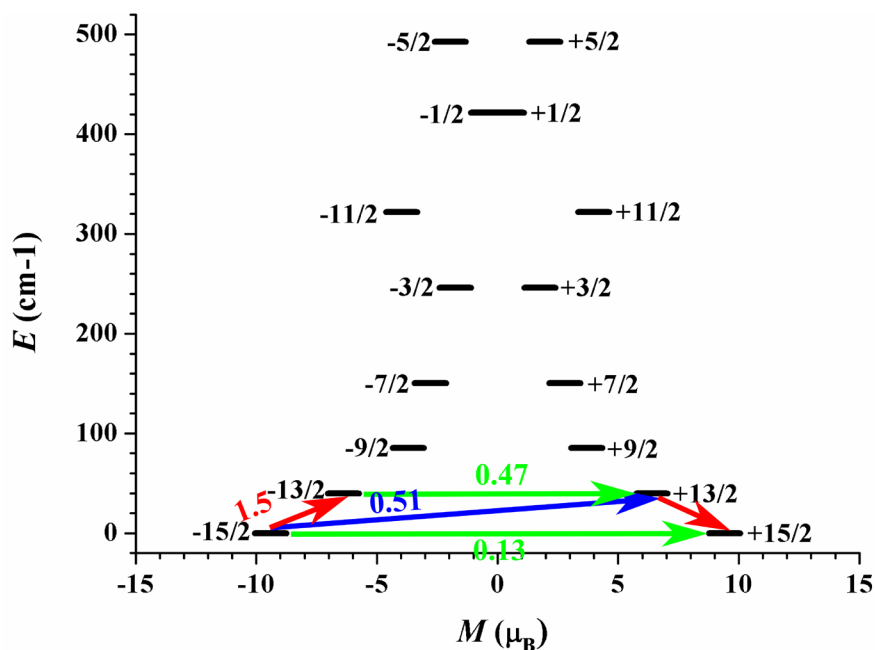
Figure S16. The magnetization blocking barriers for individual Dy^{III} fragments of **2_b**. The thick black lines represent the Kramers doublets as a function of their magnetic moment along the magnetic axis. The green lines correspond to diagonal quantum tunneling of magnetization (QTM); the blue line represent off-diagonal relaxation process. The numbers at each arrow stand for the mean absolute value of the corresponding matrix element of transition magnetic moment.

References:

[1] (a) Aquilante, F.; De Vico, L.; Ferré, N.; Ghigo, G.; Malmqvist, P.-A.; Neogrády, P.; Pedersen, T. B.; Pitonak, M.; Reiher, M.; Roos, B. O.; Serrano-Andrés, L.; Urban, M.; Veryazov, V.; Lindh, R. *J. Comput. Chem.*, 2010, **31**, 224; (b) Veryazov, V.; Widmark, P. -O.; Serrano-Andres, L.; Lindh, R.; Roos, B. O. *Int. J. Quantum Chem.*, 2004, **100**, 626; (c) Karlström, G.; Lindh, R.; Malmqvist, P. -Å.; Roos, B. O.; Ryde, U.; Veryazov, V.; Widmark, P. -O.; Cossi, M.; Schimmelpfennig, B.; Neogrády, P.; Seijo, L. *Comput. Mater. Sci.*, 2003, **28**, 222–239.

[2] Seijo, L.; Barandiarán, Z. *Computational Chemistry: Reviews of Current Trends*; World Scientific, Inc.: Singapore, 1999.

[3] (a) Chibotaru, L. F.; Ungur, L.; Soncini, A. *Angew. Chem. Int. Ed.*, 2008, **47**, 4126; (b) Ungur, L.; Van den Heuvel, W.; Chibotaru, L. F. *New J. Chem.*, 2009, **33**, 1224; (c) Chibotaru, L. F.; Ungur, L.; Aronica, C.; Elmoll, H.; Pilet, G.; Luneau, D. *J. Am. Chem. Soc.*, 2008, **130**, 12445.

[4] Lines, M. E. *J. Chem. Phys*. 1971, **55**, 2977.

[5] (a) Mondal, K. C.; Sundt, A.; Lan, Y. H.; Kostakis, G. E.; Waldmann, O.; Ungur, L.; Chibotaru, L. F.; Anson, C. E.; Powell, A. K. *Angew. Chem. Int. Ed*. 2012, **51**, 7550; (b) Langley, S. K.; Wielechowski, D. P.; Vieru, V.; Chilton, N. F.; Moubaraki, B.; Abrahams, B. F.; Chibotaru, L. F.; Murray, K. S. *Angew. Chem. Int. Ed*. 2013, **52**, 12014.